ACS OMEGA

http://pubs.acs.org/journal/acsodf

Article

Study of Codoping Effects of Ta^{5+} and Ga^{3+} on Garnet $Li_7La_3Zr_2O_{12}$

Enkhjargal Enkhbayar and JunHo Kim*

Cite This: *ACS Omega* 2022, 7, 47265−47273

Read Online

ACCESS | Metrics & More | Article Recommendations | Supporting Information

ABSTRACT: Garnet $Li_7La_3Zr_2O_{12}$ (LLZO) is a promising solid electrolyte for all-solid-state Li-ion batteries because of its outstanding performance. However, LLZO exists in two polymorphic phases, tetragonal ($\sim 10^{-3}$ mS cm^{-1}) and cubic ($1\text{-}10^{-1}$ mS cm^{-1}), where the cubic phase exhibits higher Li-ion conductivity but is thermodynamically unstable at ambient room temperature. To stabilize the cubic phase with high ionic conductivity, we fabricated mono- and codoped garnet with Ta^{5+} and Ga^{3+} ($Li_{7-3x-z=6.4}Ga_xLa_3Zr_{2-z}Ta_zO_{12}$) and investigated the doping effects. The doping effects on the crystal structure and ionic conductivity were systematically investigated using X-ray diffraction, Raman scattering, scanning electron microscopy, alternative current (AC) impedance, and direct current (DC) polarization methods. The characterization results revealed that Ta-doping favors higher occupation of Li-ions on the mobile octahedral (LiO_6) site and improves ionic conductivity of the grain boundary. However, it showed poor total ionic conductivity (2.044×10^{-4} S cm^{-1} at 1100 °C for 12 h) due to the low sinterability [relative density (RD): ∼80.3%]. On the other hand, Ga-doping provides better sinterability (RD: ∼93.1%) and bulk conductivity. Considering the beneficial effects of Ga- and Ta-doping, codoped $Li_{6.4}Ga_{0.133}La_3Zr_{1.8}Ta_{0.2}O_{12}$ garnet with enhanced ionic conductivity (6.141×10^{-4} S cm^{-1}) and improved high-density microstructure (RD: ∼95.7%) was obtained.

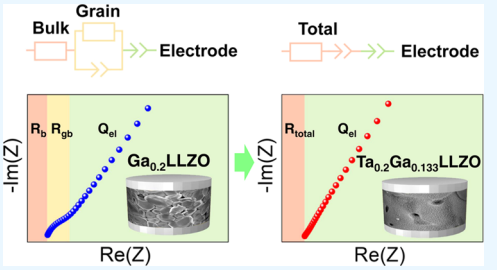

1. INTRODUCTION

In the last decades, lithium-ion batteries (LIBs) have emerged as state-of-the-art energy storage devices due to their high energy density compared with other batteries.[1−4] Nevertheless, conventional LIBs have safety issues related to carbonate-based liquid electrolytes, which limits their application to stable energy storage systems.[4,5] To solve this problem, solid inorganic electrolytes have been developed over the years, namely, Li_3N,[6] LISICON,[7,8] NASICON-type,[9] sulfide-based,[10] perovskite-type,[11] quasi-solid composite,[12,13] and garnet-type Li-ion conductors.[14,15] Among them, lithium-stuffed garnet-type $Li_7La_3Zr_2O_{12}$ (LLZO) has been studied extensively because of its remarkable performance, i.e., high ionic conductivity ($\sim 10^{-1}$ mS cm^{-1}), high chemical stability against lithium metal electrodes, wide electrochemical window (∼5 V), and low electronic conductivity.[16,17]

LLZO exists in two polymorphic forms: a tetragonal phase ($I4_1/acd$ space group) and a cubic phase ($Ia\bar{3}d$ space group). The tetragonal phase possesses high stability and poor Li-ion conductivity ($\sim 10^{-3}$ mS cm^{-1}) due to an ordered lithium sublattice with immobile tetrahedral LiO_4 (8a and 16f) and a mobile octahedral LiO_6 (32g) part, whereas the cubic phase has disordered lithium distribution over immobile tetrahedral LiO_4 (24d), mobile octahedral LiO_6 (48g and 96h) sites, and lithium vacancies, leading to higher Li-ion conductivity by 2 orders of magnitude ($\sim 10^{-1}$ mS cm^{-1}) via the improved migration pathway through low-energy sites. Unfortunately, the cubic phase of pure LLZO is thermodynamically unstable at ambient temperature.[18−21] A cation substitution with aliovalent elements has proven to be an effective way to stabilize the cubic phase by reducing the lithium content, facilitating lithium vacancies, and inducing distortions in the framework of LiO_6, ZrO_6, and LaO_8.[22,23]

Over the years, various types of substitutes have been used for structural modifications, such as Al^{3+}, Ga^{3+}, and Fe^{3+} for Li^{1+}, Sr^{2+} for La^{3+}, and Ta^{5+} and Nb^{5+} for Zr^{4+}. Among them, Al^{3+}, Ga^{3+}, and Ta^{5+} were found to be effective dopants that stabilize the cubic phase and further improve the ionic conductivity. However, the Al^{3+} dopant interferes with the migration path of lithium ions due to undesirable occupancy only in the tetrahedral LiO_4 (24d). On the other hand, Ga^{3+} and Ta^{5+} occupy tetrahedral LiO_4 (24d), octahedral LiO_6 (96h), and octahedral ZrO_6, and thus do not interfere with the movement of lithium ions.[24−28] Therefore, a preferential occupation site should be considered to obtain a better lithium migration path in the crystal structure.

In addition to the selection of the dopant for better ionic conductivity, the sintering temperature and duration are crucial parameters that play a major role in achieving a high-density microstructure and high ionic conductivity. Generally, Ta-doping requires a relatively high temperature and long

Received: October 11, 2022
Accepted: November 28, 2022
Published: December 6, 2022

sintering duration compared with Ga-doping in LLZO.[29−34] Long-time sintering at higher temperatures could induce undesirable Li loss. Therefore, it is very significant to secure a sintering process at a lower temperature and short sintering time, providing cubic-phase LLZO with suppression of Li loss. In the present study, a comparative sintering study was performed for pure LLZO, monodoped LLZO with Ga^{3+} or Ta^{5+}, and codoped LLZO ($Li_{7-3x-z=6.4}Ga_xLa_3Zr_{2-z}Ta_zO_{12}$). The pure, monodoped ($Li_{6.4}Ga_{0.2}La_3Zr_2O_{12}$ and $Li_{6.4}La_3Zr_{1.4}Ta_{0.6}O_{12}$), and codoped ($Li_{6.4}Ga_{0.067}La_3Zr_{1.6}Ta_{0.4}O_{12}$ and $Li_{6.4}Ga_{0.133}La_3Zr_{1.8}Ta_{0.2}O_{12}$) LLZO garnets were fabricated with a fixed lithium concentration of 6.4 per formula unit (pfu), which is the most suitable concentration for fast lithium diffusion.[32,35,36] For systematic comparisons, we employed various systematic characterizations such as X-ray diffraction (XRD), Raman spectroscopy, and field-emission scanning electron microscopy (FE-SEM) and correlated their results with the ionic conductivity. In particular, combined studies using XRD and Raman spectroscopy have been very rare for codoped LLZO, and our method of systematic characterization will provide deeper insights into understanding the formation of codoped LLZO garnets.

2. MATERIALS AND METHODS

2.1. Preparation. A conventional solid-state reaction method was employed to obtain pure $Li_7La_3Zr_2O_{12}$ (LLZO), monodoped LLZO ($Li_{6.4}La_3Zr_{1.4}Ta_{0.6}O_{12}$ ($Ta_{0.6}$LLZO) and $Li_{6.4}Ga_{0.2}La_3Zr_2O_{12}$ ($Ga_{0.2}$LLZO)), and codoped LLZO ($Li_{6.4}Ga_{0.133}La_3Zr_{1.6}Ta_{0.2}O_{12}$ ($Ta_{0.2}Ga_{0.133}$LLZO) and $Li_{6.4}Ga_{0.067}La_3Zr_{1.6}Ta_{0.4}O_{12}$ ($Ta_{0.4}Ga_{0.067}$LLZO)) pellets. Powders of Li_2CO_3 (99.99%, Kojundo Co. Ltd), Ga_2O_5 (99.99%, Kojundo Co. Ltd), La_2O_3 (99.9%, Sigma Aldrich), ZrO_2 (99%, Sigma Aldrich), and Ta_2O_5 (99.5%, Sigma Aldrich) were used for the synthesis of pure, monodoped, and codoped LLZO powders. To compensate for the lithium loss during the high-temperature sintering process, 25% excess Li_2CO_3 was added to the starting precursor powders. Precursor powders were mixed and milled with zirconia balls in isopropyl alcohol medium for 5 h at 700 rpm (20 cycles, 5 min rotation + 15 min break in each cycle) and then dried at 200 °C for more than 10 h. For the milling process, a planetary ball mill machine (Pulverisette 7, Fritsch) was used. The dried powder was cold-pressed (20 MPa) to form pellets and calcined at 950 °C for 6 h. After calcination, pellets were reground and repressed into pellets with 1.5−2 mm thickness for the further sintering process. To prevent Al contamination from the alumina crucible, a platinum plate was inserted between the pellet and the alumina crucible. We carried out different sintering processes: sintering at 1050 °C for 6 and 12 h and sintering at 1100 °C for 6 and 12 h. For the 12 h sintering, pellets were covered with the mother powder because Li loss and a Li-free pyrochlore $La_2Zr_2O_7$ phase were found in the pellet without covering the mother powder sintered at 1100 °C for 12 h (Figure S1). A total of six different sintering conditions were tested, but only four of them were used for further characterization.

2.2. Material Characterization. The morphology and chemical composition of the sintered pellets were examined using FE-SEM (JSM-7001F, JEOL) at an accelerating voltage of 20 kV, equipped with an energy-dispersive spectroscope (EDS, Aztec, Oxford Instruments). A few nanometers of Au were sputtered on the surface to prevent the surface-charging effect. The crystal structure was determined using a high-resolution X-ray diffraction system (HR-XRD, Smart Lab, Rigaku) in the 2θ scan mode with a scan range from 10 to 60° and a scan speed of 3° min^{-1}, using a Cu Kα (λ = 1.542 Å) line at 45 kV and 200 mA. The Raman spectroscopic measurements were carried out using a Raman spectrometer (UniRam, UninanoTech) equipped with a CCD detector (Newton 970-UVB, Andor) cooled to −60 °C, and the Rayleigh scattering wavelengths were 442 and 532 nm. The density of the pellets was calculated from their geometric dimension and weight (Figure 1).

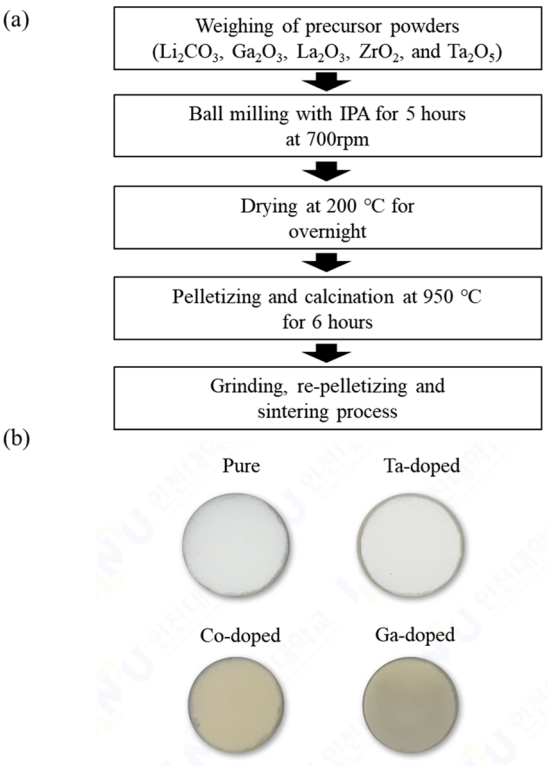

Figure 1. Schematic representation of pellet fabrication process (a) and images of sintered pellets (b).

2.3. Electrochemical Measurements. For electrodes, silver was thermally evaporated (120 nm) on both sides of the pellets in a vacuum chamber with a base pressure of 2×10^{-6} Torr. Electrochemical impedance spectroscopy (EIS) measurements were performed with a potentiostat (PGSTAT302N, Metrohm Autolab) at room temperature in the frequency range between 1 MHz and 10 Hz with 30 mV amplitude of alternative current (AC). Ionic conductivities of pellets were extracted using the following equation:

$$\sigma = \frac{d}{R \cdot A}$$

where σ is the ion conductivity, d is the thickness of the pellet, A is the area of the silver electrode, and R is the measured resistance of the pellet.

To determine the activation energy (E_a) of doped LLZO garnets, the ionic conductivity was measured in the temperature range of 20−86 °C employing the linear-fitting method according to the Arrhenius equation:

https://doi.org/10.1021/acsomega.2c06544
ACS Omega 2022, 7, 47265−47273

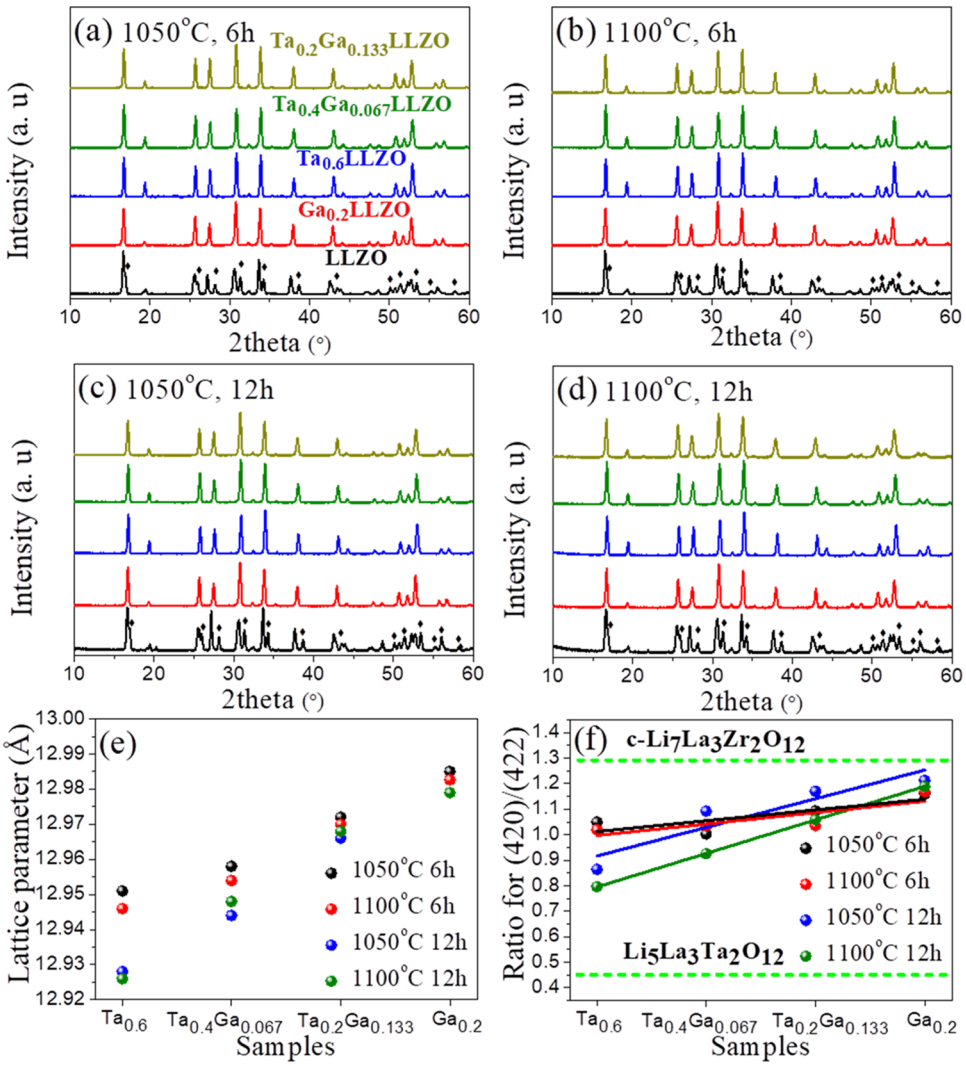

Figure 2. X-ray diffraction patterns for pure, monodoped, and codoped LLZO pellets sintered at 1050 °C for 6 h (a), 1100 °C for 6 h (b), 1050 °C for 12 h (c), and 1100 °C for 12 h (d). Lattice parameters and ratio of peaks (420)/(422) (e, f). ◆ Characteristic peaks of the tetragonal LLZO phase.

$$\sigma T = \exp\left(\frac{-E_a}{k_B T}\right)$$

where T is the measurement temperature, k_B is the Boltzmann constant, and A is the pre-exponential parameter.

The DC polarization method was employed to determine the electronic conductivity using a Keithley 2400 source meter. A polarization potential of 0.2 V was applied, and the current was recorded until it saturates for 1200 s. The electrical conductivity was calculated using the following equation:

$$\sigma_e = \frac{I_s d}{VA}$$

where V is the applied voltage and I_s is the saturation current.

3. RESULTS AND DISCUSSION

Fabricated pellets were characterized by XRD and Raman spectroscopy measurements. It is well known that the vacancy concentration of Li (0.4−0.5 pfu) is critical for the stabilization of the cubic phase.[37] According to the crystal-chemistry reaction, Ga and Ta can substitute into Li and Zr sites, respectively, as shown in the following equations:

$$Ga_2O_3 \rightarrow 2Ga_{Li}^{\bullet\bullet} + 4V'_{Li} + 3O_O^{\times}$$

$$Ta_2O_5 \rightarrow 2Ta_{Zr}^{\bullet} + 2V'_{Li} + 5O_O^{\times}$$

where $2Ga_{Li}^{\bullet\bullet}$ and $2Ta_{Zr}^{\bullet}$ represent occupations of Ga^{3+} on the site of Li^+ and Ta^{5+} on the site of Zr^{4+} with effective charges of +2 and +1, respectively. As a consequence, Li vacancies with an effective charge of −1 ($4V'_{Li}$ and $2V_{Li}'$) are created to maintain charge balance with the oxygen ($3O_O^{\times}$ and $5O_O^{\times}$) network.[27,38] In Figure 2, all doped $Li_{6.4}Ga_xLa_3Zr_{2-z}Ta_zO_{12}$ garnet samples show XRD patterns of cubic phases (Figure 2a−d),[39] while pure $Li_7La_3Zr_2O_{12}$ samples show broadened and split diffraction peaks due to their lower symmetry, which indicates the formation of the tetragonal garnet LLZO.[18] As shown in Figure 2e, the lattice parameter is reduced with more Ta^{5+} substitution due to the smaller ionic radius of Ta^{5+} (Ta^{5+}: 0.64 Å in VI coordination; Zr^{4+}: 0.72 Å in VI coordination). This result complies with Vegard's law. The decrease in lattice parameters was observed to be stronger in the pellet sintered for a longer duration. The Ta^{5+} mono- and codoped LLZO garnets sintered for 12 h exhibited a larger contraction of lattice parameters than those sintered for 6 h. On the other hand, the lattice parameters of garnets sintered for 6 h are

https://doi.org/10.1021/acsomega.2c06544
ACS Omega 2022, 7, 47265−47273

Table 1. Lattice Parameters, Relative Densities (RDs), and Ionic Conductivities of Pure, Monodoped, and Codoped LLZO

sintering condition	pellets	$a = b = c$ (Å)	relative density[a] (%)	$\sigma_{bulk}(10^{-4}$ S m$^{-1})$	$\sigma_{gb}(10^{-4}$ S m$^{-1})$	$\sigma_{total}(10^{-4}$ S m$^{-1})$
1050 °C, 6 h	LLZO	13.133 (c = 12.679)		0.017		0.017
	$Ta_{0.6}$LLZO	12.951	73.7 ± 3.7	0.319	0.150	0.102
	$Ta_{0.4}Ga_{0.067}$LLZO	12.958	87.0 ± 1.7	0.591	1.114	0.386
	$Ta_{0.2}Ga_{0.133}$LLZO	12.972	86.9 ± 3.7	0.612	0.854	0.356
	$Ga_{0.2}$LLZO	12.985	86.8 ± 0.8	1.024	0.319	0.243
1050 °C, 12 h	LLZO	13.135 (c = 12.673)		0.006	0.005	0.027
	$Ta_{0.6}$LLZO	12.928	78.3 ± 3.0	2.489	1.499	0.936
	$Ta_{0.4}Ga_{0.067}$LLZO	12.944	92.7 ± 1.3	2.772	4.154	1.662
	$Ta_{0.2}Ga_{0.133}$LLZO	12.966	93.8 ± 2.5	3.298	3.662	1.735
	$Ga_{0.2}$LLZO	12.979	90.9 ± 1.4	4.074	1.930	1.310
1100 °C, 6 h	LLZO	13.173 (c = 12.678)		0.020		0.020
	$Ta_{0.6}$LLZO	12.946	74.5 ± 4.6	0.210	0.866	0.169
	$Ta_{0.4}Ga_{0.067}$LLZO	12.954	89.4 ± 1.9	1.776	2.886	1.100
	$Ta_{0.2}Ga_{0.133}$LLZO	12.970	89.9 ± 1.1	1.959	3.039	1.191
	$Ga_{0.2}$LLZO	12.984	88.9 ± 1.2	3.539	0.893	0.713
1100 °C, 12 h	LLZO	13.165 (c = 12.698)		0.073	0.070	0.036
	$Ta_{0.6}$LLZO	12.926	80.3 ± 0.6	2.679	8.620	2.044
	$Ta_{0.4}Ga_{0.067}$LLZO	12.948	93.7 ± 1.5	3.634		3.634
	$Ta_{0.2}Ga_{0.133}$LLZO	12.968	95.7 ± 1.2	6.141		6.141
	$Ga_{0.2}$LLZO	12.979	93.1 ± 0.2	6.207	13.420	4.244

[a]Standard deviation is the average of three measurements.

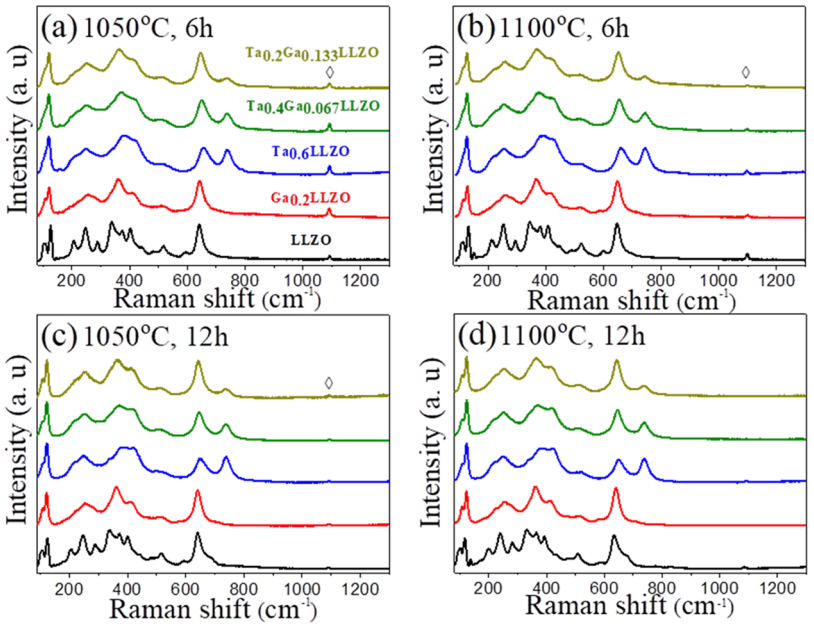

Figure 3. Raman spectra of pure, monodoped, and codoped LLZO pellets sintered at 1050 °C for 6 h (a), 1100 °C for 6 h (b), 1050 °C for 12 h (c), and 1100 °C for 12 h (d) with a Rayleigh scattering wavelength of 442 nm. ◊Characteristic peak of Li_2CO_3 (C−O stretching).

found to be similar to those sintered for 12 h with more Ga^{3+} doping. Hence, the result indicates that for Ta-doped garnets, the crystallization was highly affected by the sintering duration.

For a precise study of the Ta-doping effect, the intensity ratio of the (420) peak at ∼31° to the (422) peak at ∼34° was analyzed. The intensity ratio of (420)/(422) is 0.45 for the Zr-free garnet $Li_5La_3Ta_2O_{12}$ (LLTO),[40] whereas it is 1.3 for the nominal cubic $Li_7La_3Zr_2O_{12}$,[17] as displayed in Figure 2f with green dashed lines. This result is consistent with an increase in the peak intensity of the (422) peak with Ta^{5+} doping in the garnet structure.[34] The intensity ratio of (420)/(422) was observed to be decreased for all of the sintered samples. A linear fitting showed steeper slopes for 12 h sintering than for 6 h (Figure 2e,f). Especially, Ta-doped LLZO pellets sintered for 6 h showed a higher peak (420)/(422) intensity ratio (i.e., higher than 1.0) than those sintered for 12 h. In addition, Ta-doped LLZO pellets sintered for 6 h showed slightly larger lattice parameters (12.954−12.958 Å) (Table 1) compared

https://doi.org/10.1021/acsomega.2c06544
ACS Omega 2022, 7, 47265−47273

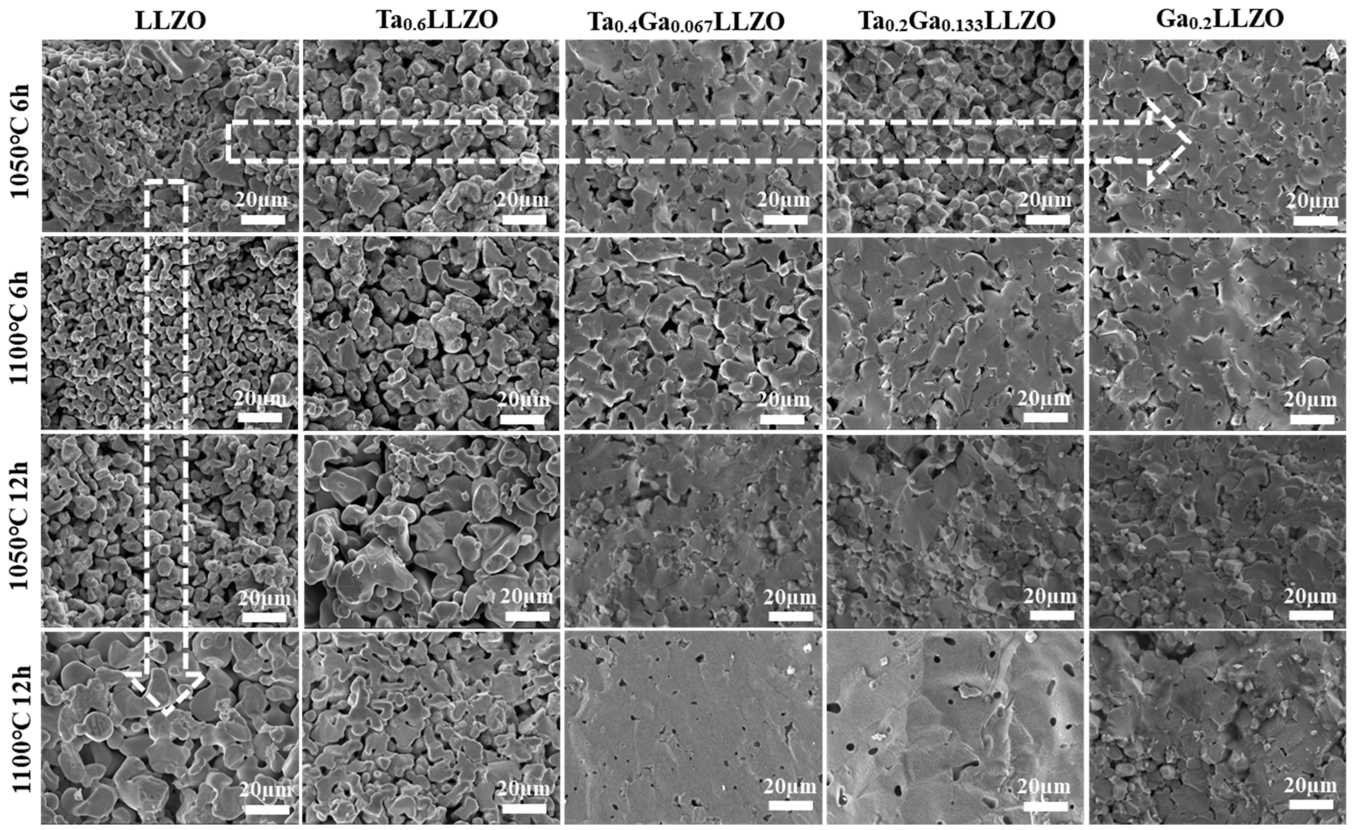

Figure 4. Cross-sectional FE-SEM images of the pure, monodoped, and codoped LLZO pellets.

with previously reported values (12.920−12.930 Å).[27,36,38] This result indicates incomplete substitution of Ta in the garnet structure, suggesting that 6 h of sintering is insufficient to completely crystallize $Ta_{0.6}$LLZO. On the other hand, $Ga_{0.2}$LLZO is reported to have a lattice parameter of 12.973 Å,[25,26] which is close to our results, indicating that 6 h sintering at 1050−1100 °C is sufficient to induce the cubic phase of Ga-doped LLZO. Our results support the fact that Ga-doping enhances crystallization at relatively low sintering temperatures and relatively shorter duration via the formation of a low-melting binary system ($LiGaO_2$−Li_5GaO_4) around 950 °C,[41] and this behavior will be discussed later.

The Raman spectra of pure, monodoped, and codoped LLZO are shown in Figure 3. Tetragonal and cubic phases of LLZO are easily distinguished by specific spectral features such as peak broadening and splitting.[42] We analyzed the Raman spectra in three frequency regions. In the low-frequency region below 300 cm^{-1}, La−O (LaO_8) and octahedral Li−O (LiO_6) stretching modes are observed in the ranges of 100−120 and 200−300 cm^{-1}, respectively. In the intermediate frequency region of 300−500 cm^{-1}, tetrahedral Li−O (LiO_4) shows the characteristic peaks of stretching modes. In the high-frequency region above 500 cm^{-1}, stretching modes of Zr−O and Ta−O in the octahedral framework show peaks at ∼650 and ∼740 cm^{-1}, respectively.[36,42] The Ta−O stretching mode at ∼740 cm^{-1} is observed for both monodoped and codoped garnets, i.e., $Ta_{0.6}$LLZO, $Ta_{0.4}Ga_{0.067}$LLZO, and $Ta_{0.2}Ga_{0.133}$LLZO, and its intensity increased with increasing Ta^{5+} content. On the other hand, the Zr−O stretching mode at ∼650 cm^{-1} gradually decreased as Ta^{5+} was substituted into the Zr^{4+} site, as shown in Figure S2. This result was in good agreement with the trend of the peak intensity ratio of (420)/(422) in the XRD result (Figure 2e). Further, the peak areas of the Ta−O and Zr−O stretching modes were used to estimate element concentrations. By fitting the curves with the Lorentzian function, the ratios of [Ta]/([Ta] + [Zr]) were calculated, and the result is shown in Table S1. The [Ta]/([Ta] + [Zr]) ratios were calculated to be 0.3, 0.2, and 0.1 for $Ta_{0.6}$LLZO, $Ta_{0.4}Ga_{0.067}$LLZO, and $Ta_{0.2}Ga_{0.133}$LLZO, respectively, which are consistent with the EDS results (Table S4).

To understand the ion conductivity via the Raman spectroscopy, analysis of the LiO_6 stretching mode (at 200−300 cm^{-1}) is important. Thus, we performed a qualitative analysis of the spectra in the frequency range of 200−500 cm^{-1}. Higher lithium occupation at mobile octahedral LiO_6 and a disordered arrangement of lithium occupation are known to be beneficial for high ionic conduction.[20,36] Lithium ions distribute over LiO_4 (24d) and LiO_6 (96h) sites with occupation concentrations of 55 and 39%, respectively, when the Ga-doping concentration is x = 0.3 pfu.[17] On the other hand, lithium ions occupy tetrahedral LiO_4 (24d) and octahedral LiO_6 (48g and 96h) sites with occupation concentrations of 38 and 52% (28% at 48g and 24% at 96h), respectively, when the Ta^{5+} doping concentration is z = 0.5 pfu.[32,36] Therefore, Ta^{5+} doping has a better effect on disordered lithium distribution and the number of mobile lithium ions in octahedral LiO_6 (48g and 96h) sites. With peak intensities of ∼251 cm^{-1} (LiO_6) and ∼363 cm^{-1} (LiO_4), [LiO_6]/([LiO_6] + [LiO_4]) ratios were calculated, and the results are shown in Table S2. The ratios were estimated to be 0.39, 0.42, 0.41, and 0.37 for $Ta_{0.6}$LLZO, $Ta_{0.4}Ga_{0.067}$LLZO, $Ta_{0.2}Ga_{0.133}$LLZO, and $Ga_{0.2}$LLZO at 1100 °C for 12 h, respectively, and the ratio is observed to increase with Ta-doping under all sintering conditions. This result shows that

https://doi.org/10.1021/acsomega.2c06544
ACS Omega 2022, 7, 47265−47273

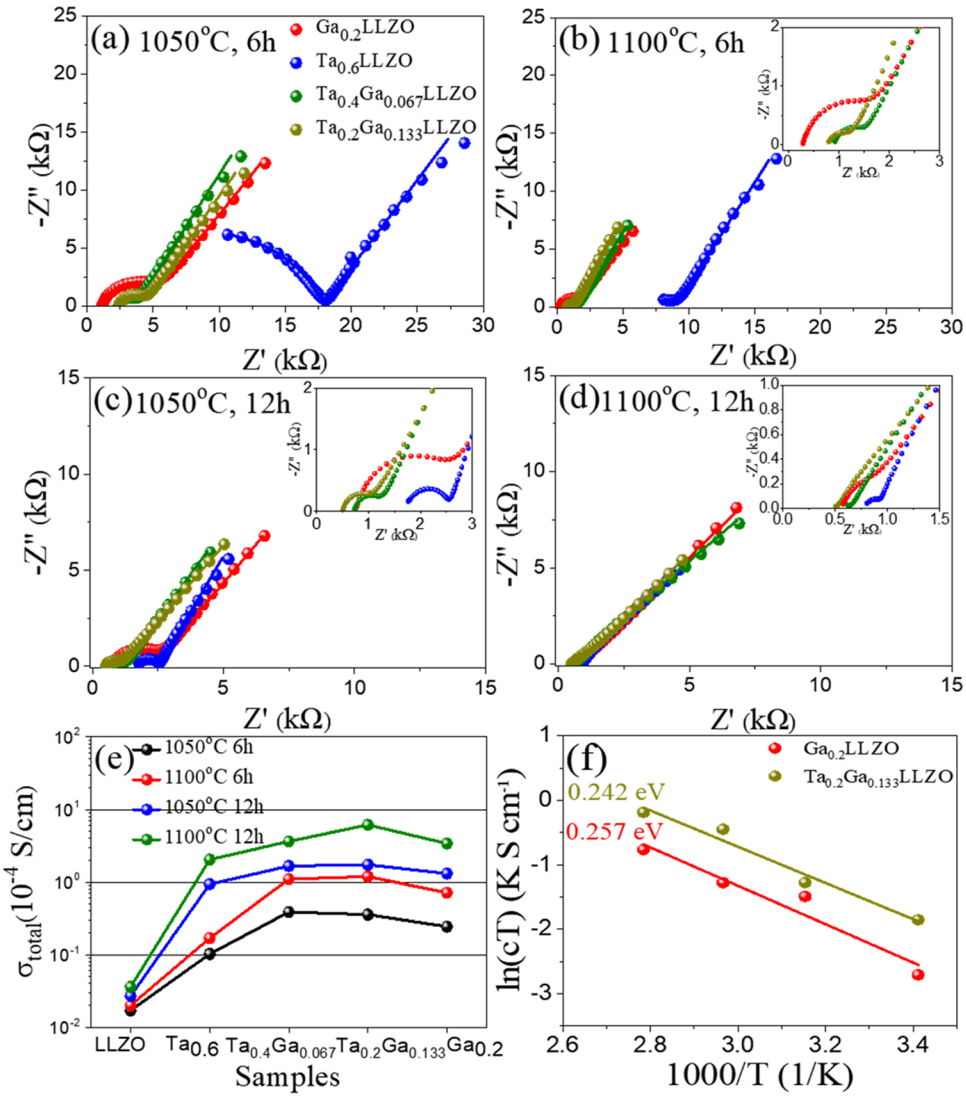

Figure 5. EIS measurement results for pure, monodoped, and codoped LLZO pellets sintered at 1050 °C for 6 h (a), 1100 °C for 6 h (b), 1050 °C for 12 h (c), and 1100 °C for 12 h (d); summary of the total ion conductivity (e) and the Arrhenius plots (f) of selected garnets.

Ta-doping enables better lithium occupation at mobile LiO_6 than Ga-doping.[37]

The Li_2CO_3 phase is known to have negative effects on the device performance and stability of solid-state batteries. It increases the interlayer resistance between lithium metal and LLZO (Li|LLZO) garnets and decreases the densification of solid-state garnet electrolytes, which deteriorates the device performance by lowering the ionic conductivity and degrading cyclic performance.[43−46] The symmetric stretching C−O mode of Li_2CO_3 at ∼1090 cm^{-1} is observed in Figure S2.[47,48] We calculated the [C]/([C] + [La]) ratio in the same way to estimate the [Ta]/([Ta] + [Zr]) ratio from the Raman spectra. As shown in Table S3, the ratios were estimated to be 0.20, 0.21, 0.21, and 0.22 at 950 °C for 6 h-calcined $Ta_{0.6}$LLZO, $Ta_{0.4}Ga_{0.067}$LLZO, $Ta_{0.2}Ga_{0.133}$LLZO, and $Ga_{0.2}$LLZO, respectively, which are close to the amount of excess Li_2CO_3 in the starting powder. The ratio of [C]/([C] + [La]) was calculated to be reduced to 0.09, 0.09, 0.08, and 0.10 at 1050 °C for 6 h-sintered $Ta_{0.6}$LLZO, $Ta_{0.4}Ga_{0.067}$LLZO, $Ta_{0.2}Ga_{0.133}$LLZO, and $Ga_{0.2}$LLZO, respectively. Furthermore, for pellets sintered at 1100 °C for 12 h, the Li_2CO_3 phase significantly reduced to 0.04 and 0.01 for $Ta_{0.6}$LLZO and $Ga_{0.2}$LLZO, respectively, and also, no trace was observed for $Ta_{0.4}Ga_{0.067}$LLZO and $Ta_{0.2}Ga_{0.133}$LLZO. From this result, we expect high ionic conductivity for $Ta_{0.4}Ga_{0.067}$LLZO and $Ta_{0.2}Ga_{0.133}$LLZO, and this is highly consistent with the ion conductivity result.

Figure 4 shows the cross-sectional microstructure of pure, monodoped, and codoped LLZO garnets. As shown in the figure, the densification process was not initiated for all of the $Ta_{0.6}$LLZO garnets. The result indicates that either a high temperature or a long sintering duration is required to densify the Ta-doped LLZO.[49−51] However, a denser grain structure was obtained with Ga-doping, which is associated with the formation of a binary system ($LiGaO_2$−Li_5GaO_4). The binary compound is known to form and wet the garnet particles to promote densification even at relatively low sintering temperatures (950 °C).[41] The densification of the grain structure via Ga-doping was possible even with a small amount of Ga^{3+} (x = 0.05 pfu) in the garnet system.[38] $Ta_{0.4}Ga_{0.067}$LLZO, $Ta_{0.2}Ga_{0.133}$LLZO, and $Ga_{0.2}$LLZO pellets sintered at 1100 °C for 12 h showed the most compact and dense microstructure compared with the rest of the fabricated garnets. Among them, the codoped garnet $Ta_{0.2}Ga_{0.133}$LLZO (1100 °C,

https://doi.org/10.1021/acsomega.2c06544
ACS Omega 2022, 7, 47265−47273

12 h) exhibited highly reduced grain boundaries and showed the highest relative density (RD) (Table 1).

Figure 5 displays Nyquist plots for the samples that were sintered under the following conditions: 1050 °C for 6 h (Figure 5a), 1100 °C for 6 h (Figure 5b), 1050 °C for 12 h (Figure 5c), and 1100 °C for 12 h (Figure 5d) and total ionic conductivity (Figure 5). The impedance spectra were fitted using three different equivalent circuits (Figure S4) based on the AC response curves. (i) The pure LLZO garnets sintered for 12 h were fitted with the $[(R_bQ_b)(R_{gb}Q_{gb})Q_{el}]$ equivalent circuit. (ii) For most cases, impedance spectra of doped LLZOs showed a single semicircular arc in the high-frequency region and a tail in the low-frequency region due to Ag-ion-blocking electrodes.[52,53] Thus, the $[R_b(R_{gb}Q_{gb})Q_{el}]$ equivalent circuit was employed, where R_b and R_{gb} represent the resistance of the bulk and grain boundary (GB) and Q_{gb} and Q_{el} are constant phase element contributions to the grain boundary (GB) and electrode, respectively. (iii) The garnets ($Ta_{0.4}Ga_{0.067}$LLZO and $Ta_{0.2}Ga_{0.133}$LLZO) sintered at 1100 °C for 12 h showed a negligible semicircular (Figure 5d inset) arc, and their spectra were fitted with $[R_{total}Q_{total}Q_{el}]$, where R_{total} is the sum of R_b and R_{gb}. Figure 5e,f summarizes the ion conductivity and the Arrhenius plots of selected garnets and will be discussed with EIS results later.

EIS measurement results revealed the following interesting points. First, the radius of the semicircle was reduced almost by half as the sintering temperature was elevated by 50 °C (Figure 5a,b) for all samples, indicating that the total ionic conductivities were increased from 0.017, 0.102, 0.386, 0.356, and 0.243 × 10^{-4} S cm^{-1} to 0.020, 0.169, 1.100, 1.191, and 0.713 × 10^{-4} S cm^{-1} for LLZO, $Ta_{0.6}$LLZO, $Ta_{0.4}Ga_{0.067}$LLZO, $Ta_{0.2}Ga_{0.133}$LLZO, and $Ga_{0.2}$LLZO, respectively. On the other hand, doubling the sintering duration (Figure 5c) had a much better effect on the crystallization of the cubic garnet structure; thus, the total ionic conductivities were increased up to 0.027, 0.936, 1.662, 1.735, and 1.310 × 10^{-4} S cm^{-1} for LLZO, $Ta_{0.6}$LLZO, $Ta_{0.4}Ga_{0.067}$LLZO, $Ta_{0.2}Ga_{0.133}$LLZO, and $Ga_{0.2}$LLZO, respectively. Second, Ga-doping had different effects on the bulk and GB conductivities. As shown in the tabulated ionic conductivity results (Table 1), ion conductivity in the bulk improves as the concentration of Ga^{3+} increases from 0 to 0.2 pfu due to Ga^{3+} sinterability,[28,37,41] whereas the ion conductivity in the grain boundary decreases with increasing Ga^{3+} (x = 0.067−0.2 pfu). For Ta-doping, in addition to the effect on stabilizing the cubic phase and introducing lithium vacancies and distortions,[54] a low Ta^{5+} (z < 0.6 pfu) content is helpful for structural densification and reduction of grain boundaries,[36] but it requires strong sintering conditions (higher sintering temperature and longer sintering time) as mentioned earlier. For this reason, Ta-doped LLZO showed poor Li-ion conductivity and a coarse microstructure under mild sintering conditions. Third, codoped garnets, $Ta_{0.4}Ga_{0.067}$LLZO (3.634 × 10^{-4} S cm^{-1}) and $Ta_{0.2}Ga_{0.133}$LLZO (6.141 × 10^{-4} S cm^{-1}), which were sintered at 1100 °C for 12 h (Figure 5d), did not show any clear semicircles in the high-frequency region but only tails in the low-frequency region. This result suggests negligible resistance at the GB compared with the bulk, being in good agreement with previously reported results.[55,56] With the help of the Ga-containing binary $LiGaO_2$−Li_5GaO_4 system and under moderate sintering conditions (1100 °C, 12 h), Ta-doping enhanced the densification and microstructure of grains. Thereby, transgranular fracture was observed in the flat fracture surfaces of $Ta_{0.4}Ga_{0.067}$LLZO and $Ta_{0.2}Ga_{0.133}$LLZO (Figure 4) due to the high grain boundary strength, which facilitates low intergranular ion resistance between GBs; as a result, it showed enhanced total ionic conductivity (Figure 5e).[24,55,56]

The electronic conductivities (σ_e) of mono- and codoped LLZO (1100 °C, 12 h) garnets were characterized by the DC polarization method, and the results are shown in Figure 6.

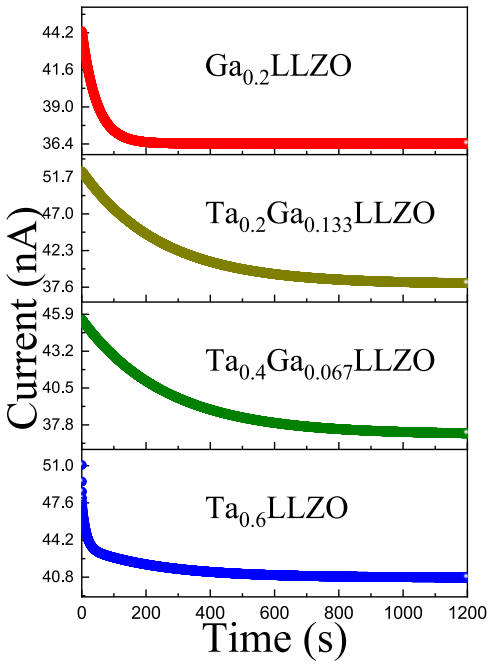

Figure 6. DC polarization curves for mono- and codoped LLZO.

Even though electrical conduction is amplified with increasing Ga doping from x = 0 to 0.2, the values of electronic conductions were on the order of 10^{-8} S cm^{-1}, which is 4 orders of magnitude lower than the lithium ion conductivity. As a consequence, the lithium ion transference number $t_{Li} = \frac{\sigma_{total} + \sigma_e}{\sigma_{total}}$ for the mono- and codoped LLZO is nearly unity (Table S5).

Finally, the highest total ion conductivity achieved was up to 6.141 × 10^{-4} S cm^{-1} for the $Ta_{0.2}Ga_{0.133}$LLZO sintered at 1100 °C for 12 h (Figure 5e). The higher ion conductivity of $Ta_{0.2}Ga_{0.133}$LLZO is ascribed to improved lithium distribution, dense microstructure, reduced grain boundaries, and reduced activation energy (0.242 eV) compared with the Ga-doped garnet $Ga_{0.2}$LLZO (0.257 eV), as shown in Figure 5f.

4. CONCLUSIONS

In summary, the influence of codoping (Ta^{5+} and Ga^{3+}) on the properties of $Li_{7-3x-z=6.4}Ga_xLa_3Zr_{2-z}Ta_zO_{12}$ garnets was investigated. We carried out systematic characterizations of the fabricated pellets to gain a deeper understanding of their ionic conductivities. The Raman spectroscopy combined with XRD and FE-SEM turned out to be very effective to obtain detailed information on the crystal structure of the doped LLZO. The characterization studies revealed the following results: (i) The cubic phase was obtained for all mono- and codoped LLZO garnets at a lower temperature and shorter duration compared with pure LLZO. (ii) Ta-doped garnets ($Ta_{0.6}$LLZO, $Ta_{0.4}Ga_{0.067}$LLZO, and $Ta_{0.2}Ga_{0.133}$LLZO)

https://doi.org/10.1021/acsomega.2c06544
ACS Omega 2022, 7, 47265−47273

showed a higher ratio of $[LiO_6]/([LiO_6] + [LiO_4])$ than $Ga_{0.2}$LLZO because of the enhanced Li-ion distribution on mobile LiO_6 sites. However, $Ta_{0.6}$LLZO required either a higher sintering temperature or a longer duration to promote the densification process, whereas Ga-doped garnets ($Ta_{0.4}Ga_{0.067}$LLZO, $Ta_{0.2}Ga_{0.133}$LLZO, and $Ga_{0.2}$LLZO) easily induced densification of the garnet pellets due to its good sinterability. (iii) The codoped garnet $Ta_{0.2}Ga_{0.133}$LLZO showed relativity higher ionic conductivity compared with its counterparts ($Ta_{0.6}$LLZO, $Ta_{0.4}Ga_{0.067}$LLZO, and $Ga_{0.2}$LLZO) because of the improved Li distribution, dense microstructures, reduced activation energy, and grain boundary. Therefore, the highest ionic conductivity of 6.141×10^{-4} S cm^{-1} was obtained, and further enhancement is expected by optimizing the sintering conditions for $Ta_{0.2}Ga_{0.133}$LLZO.

■ ASSOCIATED CONTENT

Supporting Information

The Supporting Information is available free of charge at https://pubs.acs.org/doi/10.1021/acsomega.2c06544.

XRD and Raman spectra for LLZO garnets sintered at 1100 °C for 12 h without the mother powder covering; Raman spectra for calcinated garnets; peak ratio table for Zr−O and Ta−O stretching modes; mobile LiO_6 and immobile LiO_4 modes and peak ratios for La−O (LLZO) and C−O (Li_2CO_3) stretching modes; EDS mapping images for doped LLZO; equivalent circuits for AC impedance; table for activation energy, electric conductivity, and ion transference number for doped LLZO (PDF)

■ AUTHOR INFORMATION

Corresponding Author

JunHo Kim − *Department of Physics, Incheon National University, Yeonsu-gu, Incheon 22012, Republic of Korea;* orcid.org/0000-0002-2204-7163; Email: jhk@inu.ac.kr

Author

Enkhjargal Enkhbayar − *Department of Physics, Incheon National University, Yeonsu-gu, Incheon 22012, Republic of Korea*

Complete contact information is available at: https://pubs.acs.org/10.1021/acsomega.2c06544

Notes

The authors declare no competing financial interest.

■ ACKNOWLEDGMENTS

This study was supported by the Incheon National University Research Grant in 2021.

■ REFERENCES

(1) Scrosati, B. History of lithium batteries. *J. Solid State Electrochem.* **2011**, *15*, 1623−1630.

(2) Tarascon, J.-M.; Armand, M. Issues and challenges facing rechargeable lithium batteries. *Nature* **2001**, *414*, 359−367.

(3) Placke, T.; Kloepsch, R.; Dühnen, S.; Winter, M. Lithium ion, lithium metal and alternative rechargeable battery technologies: the odyssey for high energy density. *J. Solid State Electrochem.* **2017**, *21*, 1939−1964.

(4) Xu, K. Nonaqueous liquid electrolytes for lithium-based rechargeable batteries. *Chem. Rev.* **2004**, *104*, 4303−4418.

(5) Kalhoff, J.; Eshetu, G. G.; Bresser, D.; Passerini, S. Safer electrolytes for lithium-ion batteries: State of the art and perspectives. *ChemSusChem* **2015**, *8*, 2154−2175.

(6) Rabenau, A.; Schulz, H. Re-evaluation of the lithium nitride structure. *J. Less Common Met.* **1976**, *50*, 155−159.

(7) Hong, H. Y. P. Crystal structure and ionic conductivity of $Li_{14}Zn(GeO_4)$ and other new Li^+ superionic conductors. *Mater. Res. Bull.* **1978**, *13*, 117−124.

(8) Kanno, R.; Murayama, M. Lithium ionic conductor Thio-LISICON: The Li_2S GeS_2 P_2S_5 system. *J. Electrochem. Soc.* **2001**, *148*, A742−A746.

(9) Aono, H.; Sugimoto, E.; Sadaoka, Y.; Imanaka, N.; Adachi, G. Y. Ionic conductivity of solid electrolytes based on lithium titanium phosphate. *J. Electrochem. Soc.* **1990**, *137*, 1023−1027.

(10) Trevey, J. E.; Jung, Y. S.; Lee, S. H. High lithium ion conducting Li_2S-GeS_2-P_2S_5 glass-ceramic solid electrolyte with sulfur additive for all solid-state lithium secondary batteries. *Electrochim. Acta* **2011**, *56*, 4243−4247.

(11) Inaguma, Y.; Nakashima, M. A rechargeable lithium-air battery using lithium ion-conducting lanthanum lithium titanate ceramics as an electrolyte separator. *J. Power Sci.* **2013**, *228*, 250−255.

(12) Yanfang, Z.; Guanming, Y.; Zhong, Z.; Shufeng, S.; Shua, L.; Ning, H.; Weiping, T.; Zhaoyin, W.; Li, L.; Janina, M. Composite Hybdrid Quasi-Solid Electrolyte for High-Energy Lithium Metal Batteries. *ACS Appl. Energy Mater.* **2021**, *4*, 7973−7982.

(13) Guanming, Y.; Yanfang, Z.; Jianyao, Y.; Shufeng, S.; Liyang, L.; Weiping, T.; Zhaoyin, W.; Ning, H.; Li, L. Synthesis and properties of poly(1,3-dioxalane) *in situ* quasi-solid-state electrolytes *via* a rare-earth triflate catalyst. *Chem. Commun.* **2021**, *57*, 7034.

(14) Thangadurai, V.; Narayanana, S.; Pinzarua, D. Garnet-type solid-state fast Li ion conductors for Li batteries: critical review. *Chem. Soc. Rev.* **2014**, *43*, 4714−4727.

(15) Samson, A. J.; Hofstetter, K.; Baga, S.; Thangadurai, V. A bird's-eye view of Li-stuffed garnet-type $Li_7La_3Zr_2O_{12}$ ceramic electrolytes for advanced all-solid-state Li batteries. *Energy Environ. Sci.* **2019**, *12*, 2957−2975.

(16) Murugan, R.; Thangadurai, V.; Weppner, W. Fast lithium ion conduction in garnet-type $Li_7La_3Zr_2O_{12}$. *Angew. Chem., Int. Ed.* **2007**, *46*, 7778−7781.

(17) Wu, J. F.; Pang, W. K.; Peterson, V. K.; Wei, L.; Guo, X. Garnet-type fast Li-ion conductors with high ionic conductivities for All-Solid-State batteries. *ACS Appl. Mater. Interfaces* **2017**, *9*, 12461−12468.

(18) Geiger, C. A.; Alekseev, E.; Lazic, B.; Fisch, M.; Armbruster, T.; Langner, R.; Fechtelkord, M.; Kim, N.; Pettke, T.; Weppner, W. Crystal chemistry and stability of "$Li_7La_3Zr_2O_{12}$" garnet: a fast lithium-ion conductor. *Inorg. Chem.* **2011**, *50*, 1089−1097.

(19) Buschmann, H.; Dolle, J.; Berendts, S.; Kuhn, A.; Bottke, P.; Wilkening, M.; Heitjans, P.; Senyshyn, A.; Ehrenberg, H.; Lotnyk, A.; Duppel, V.; Kienle, L.; Janek, J. Structure and dymanics of the fast lithium ion conductor "$Li_7La_3Zr_2O_{12}$". *Phys. Chem. Chem. Phys.* **2011**, *13*, 19378−19392.

(20) Awaka, J.; Akira, T.; Kunimitsu, K.; Norihito, K.; Yasushi, I.; Junji, A. Crystal structure of fast lithium-ion-conducting cubic $Li_7La_3Zr_2O_{12}$. *Chem. Lett.* **2011**, *40*, 60−62.

(21) Miara, L. J.; Ong, S. P.; Mo, Y.; Richards, W. D.; Park, Y.; Lee, J. -M.; Lee, H. S.; Ceder, G. Effect of Rb and Ta Doping on the Ionic Conductivity and Stability of the Garnet $Li_{7+2x-y}(La_{3-x}Rb_x)$-$(Zr_{2-y}Ta_y)O_{12}$ ($0 \le x \le 0.375$, $0 \le y \le 1$) Superionic Conductor: A First Principles Investigation. *Chem. Mater.* **2013**, *25*, 3048−3055.

(22) Mukhopadhyay, S.; Thompson, T.; Sakamoto, J.; Huq, A.; Wolfenstine, J.; Allen, J. L.; Bernstein, N.; Stewart, D. A.; Johannes, M. D. Structure and Stoichiometry in Supervalent Doped $Li_7La_3Zr_2O_{12}$. *Chem. Mater.* **2015**, *27*, 3658−3665.

(23) Shen, X.; Zhang, Q.; Ning, T.; Liu, T.; Luo, Y.; He, X.; Luo, Z.; Lu, A. Critical challenges and progress of solid garnet electrolytes for all-solid-state batteries. *Mater. Today Chem.* **2020**, *18*, No. 100368.

(24) Rangasamy, E.; Wolfenstine, J.; Sakamoto, J. The role of Al and Li concentration on the formation of cubic garnet solid electrolyte of

nominal composition $Li_7La_3Zr_2O_{12}$. *Solid State Ionics* **2012**, *206*, 28−32.
(25) Wu, J. F.; Chen, E. Y.; Yu, T.; Liu, L.; Wu, Y.; Pang, W. K.; Peterson, V. K.; Guo, X. Gallium-Doped $Li_7La_3Zr_2O_{12}$ Garnet-Type Electrolytes with High Lithium-Ion Conductivity. *ACS Appl. Mater. Interfaces* **2017**, *9*, 1542−1552.
(26) Shen, L.; Wang, L.; Wang, Z.; Jin, C.; Peng, L.; Pan, X.; Sun, J.; Yang, R. Preparation and characterization of Ga and Sr co-doped $Li_7La_3Zr_2O_{12}$ garnet-type solid electrolyte. *Solid State Ionics* **2019**, *339*, No. 114992.
(27) Yi, M.; Liu, T.; Wang, X.; Li, J.; Wang, Ch.; Mo, Y. High densification and Li-ion conductivity of Al-free $Li_{7-x}La_3Zr_{2-x}Ta_xO_{12}$ garnet solid electrolyte prepared by using ultrafine powders. *Ceram. Int.* **2019**, *45*, 786−792.
(28) Lan, W.; Fan, H.; Lau, V. W.; Zhang, J.; Zhang, J.; Zhao, R.; Chen, H. Realizing $Li_7La_3Zr_2O_{12}$ garnets with high Li^+ conductivity and dense microstructures by Ga/Nb dual substitution for lithium solid-state battery applications. *Sustainable Energy Fuels* **2020**, *4*, 1812−1821.
(29) Yi, M.; Liu, T.; Li, J.; Wang, C.; Mo, Y.; Wang, X.; Wei, Y. High Li-ion conductivity of Al-free $Li_{7-3x}Ga_xLa_3Zr_2O_{12}$ solid electrolyte prepared by liquid-phase sintering. *J. Solid State Electrochem.* **2019**, *23*, 1249−1256.
(30) Su, J.; Huang, X.; Huan, X.; Song, Z.; Xiu, T.; Badding, M. E.; Jin, J. Overcoming the abnormal grain growth in Ga-doped $Li_7La_3Zr_2O_{12}$ to enhance the electrochemical stability against Li metal. *Ceram. Int.* **2019**, *45*, 14991−14996.
(31) Lopez, C. B.; Manalastas, W.; Lopez del Amo, J. M.; Aguandero, A.; Aguesse, F.; Kilner, J. A. Atmosphere controlled processing of Ga-substituted garnets for high Li-ion conductivity. *Chem. Mater.* **2014**, *26*, 3610−3617.
(32) Li, Y.; Han, J. T.; Wang, C. A.; Xie, H.; Goodenough, J. B. Optimizing Li^+ conductivity in a garnet framework. *J. Mater. Chem.* **2012**, *22*, 15357−15361.
(33) Liu, K.; Ma, J. T.; Wang, C. A. Excess lithium salt functions more than compensating for lithium loss when synthesizing $Li_{6.5}La_3Ta_{0.5}Zr_{1.5}O_{12}$ in alumina crucible. *J. Power Sources* **2014**, *260*, 109−144.
(34) Xiang, X.; Chen, F.; Yang, W.; Yang, J.; Ma, X.; Chen, D.; Su, K.; Shen, Q.; Zhang, L. Dual regulation of Li+ migration of $Li_{6.5}La_3Zr_{1.4}M_{0.6}O_{12}$ (M = Sb, Ta, Nb) by bottleneck size and bond length of M-O. *J. Am. Ceram. Soc.* **2020**, *103*, 2483−2490.
(35) Zeier, W. G. Structural limitations for optimizing garnet-type solid electrolytes: a perspective. *Dalton Trans.* **2014**, *43*, 16133−16138.
(36) Zhang, Y.; Deng, J.; Hu, D.; Chen, F.; Shen, Q.; Zhang, L.; Dong, S. Synergistic regulation of garnet-type Ta-doped $Li_7La_3Zr_2O_{12}$ solid electrolyte by Li^+ concentration and Li^+ transport channel size. *Electrochim. Acta* **2019**, *296*, 823−829.
(37) Thompson, T.; Wolfenstine, J.; Allen, J. L.; Johannes, M.; Huq, A.; David, I. N.; Sakamoto, J. Tetragonal vs. cubic phase stability in Al-free Ta doped $Li_7La_3Zr_2O_{12}$ (LLZO). *J. Mater. Chem. A* **2014**, *2*, 13431−13436.
(38) Chen, C.; Sun, Y.; He, L.; Kotobuki, M.; Hanc, E.; Chen, Y.; Zeng, K.; Lu, L. Microstructural and Electrochemical Properties of Al- and Ga-Doped $Li_7La_3Zr_2O_{12}$ Garnet Solid Electrolytes. *ACS Appl. Energy Mater.* **2020**, *3*, 4708−4719.
(39) Xie, H.; Alonso, J. A.; Li, Y.; Fernandez-Diaz, M. T.; Goodenough, J. B. Lithium distribution in aluminum-free cubic $Li_7La_3Zr_2O_{12}$. *Chem. Mater.* **2011**, *23*, 3587−3589.
(40) Cussen, E. J. The structure of lithium garnets: cation disorder and clustering in a new family of fast Li^+ conductors. *Chem. Commun.* **2006**, 412−413.
(41) Matsuda, Y.; Sakaida, A.; Sugimoto, K.; Mori, D.; Takeda, Y.; Yamamoto, O.; Imanishi, N. Sintering behavior and electrochemical properties of garnet-like lithium conductor $Li_{6.25}M_{0.25}La_3Zr_2O_{12}$(M: $Al^{3+}$and Ga^{3+}). *Solid State Ionics* **2017**, *311*, 69−74.
(42) Tietz, F.; Wegener, T.; Gerhards, M. T.; Giarola, M.; Mariotto, G. Synthesis and Raman micro-spectroscopy investigation of $Li_7La_3Zr_2O_{12}$. *Solid State Ionics* **2013**, *230*, 77−82.
(43) Yixuan, G.; Jun, C.; Zhen, Z.; Yuanyuan, Li.; Hongqiang, Z.; Deping, L.; Lijie, C. Li_2CO_3: Insights into its Blocking Effect on Li-ion Transfer in Granet Composite Electrolytes. *ACS Appl. Energy Mater.* **2022**, *5*, 2853−2861.
(44) Huo, H.; Jing, L.; Venkataraman, T.; Xiangxin, G.; Ce-Wen, N.; Xueliang, S. Li_2CO_3: A Critical Issue for Developing Solid Garnet Batteries. *ACS Energy Lett.* **2020**, *5*, 252−262.
(45) Alexander, A. D.; Jonas, K. S.; Adam, H. Decomposition of Trace Li2CO3 During Charging Leads to Cathode Interface Degradation with the Solid Electrolyte LLZO. *Adv. Funct. Mater.* **2021**, *31*, No. 2103716.
(46) Sharafi, A.; Eric, K.; Andrew, L. D.; Seungho, Yu.; Travis, T.; Donald, J. S.; Neil, P. D.; Jeff, S. Surface Chemistry Mechanism of Ultra-Low Interfacial Resistance in the Solid-State Electrolyte $Li_7La_3Zr_2O_{12}$. *Chem. Mater.* **2017**, *29*, 7961−7968.
(47) Brooker, M. H.; Bates, J. Raman and Infrared Spectral Studies of Anhydrous Li_2CO_3 and Na_2CO_3. *J. Chem. Phys.* **1971**, *54*, 4788.
(48) Peltzer, D.; John, M.; Laura, C. Operando Raman spectroscopic studies of lithium zirconates during CO_2 capture at high temperature. *RSC Adv.* **2016**, *6*, 8222.
(49) Yang, L.; Dai, Q.; Liu, L.; Shao, D.; Luo, K.; Jamil, S.; Liu, H.; Luo, Z.; Chang, B.; Wang, X. Rapid sintering method for highly conductive $Li_7La_3Zr_2O_{12}$ ceramic electrolyte. *Ceram. Int.* **2020**, *46*, 10917−10924.
(50) Gong, Y.; Liu, Z. G.; Jin, Y. J.; Ouyang, J. H.; Chen, L.; Wang, Y. J. Effect of sintering process on the microstructure and ionic conductivity of $Li_{7-x}La_3Zr_{2-x}Ta_xO_{12}$ ceramics. *Ceram. Int.* **2019**, *45*, 18439−18444.
(51) Nonemacher, J. F.; Hüter, C.; Zheng, H.; Malzbender, J.; Krüger, M.; Spatschek, R.; Finsterbusc, M. Microstructure and properties investigation of garnet structured $Li_7La_3Zr_2O_{12}$ as electrolyte for all-solid-state batteries. *Solid State Ionics* **2018**, *321*, 126−134.
(52) Jamnik, J.; Maier, J. Treatment of the Impedance of Mixed Conductors Equivalent Circuit Model and Explicit Approximate Solutions. *J. Electrochem. Soc.* **1999**, *146*, 4183−4188.
(53) Raistrick, I. D.; Ho, C.; Huggins, R. A. Ionin conductivity of Some Lithiun Silicates and Aluminosilicates. *J. Electrochen. Soc* **1976**, *123*, 1469.
(54) Mukhopadhyay, S.; Thompson, T.; Sakamoto, J.; Huq, A.; Wolfenstine, J.; Allen, J. L.; Bernstein, N.; Stewart, D. A.; Johannes, M. D. Structure and stoichiometry in supervalent doped $Li_7La_3Zr_2O_{12}$. *Chem. Mater.* **2015**, *27*, 3658−3665.
(55) Wolfenstine, J.; Ratchford, J.; Rangasamy, E.; Sakamoto, K.; Allen, J. L. Synthesis and high Li-ion conductivity of Ga-stabilized cubic $Li_7La_3Zr_2O_{12}$. *Mater. Chem. Phys.* **2012**, *134*, 571−575.
(56) Allen, J. L.; Wolfenstine, J.; Rangasamy, E.; Sakamoto, J. Effect of substitution (Ta, Al, Ga) on the conductivity of $Li_7La_3Zr_2O_{12}$. *J. Power Sources* **2012**, *206*, 315−319.

https://doi.org/10.1021/acsomega.2c06544
ACS Omega 2022, 7, 47265−47273